

Two-point spectral model for variable-density homogeneous turbulenceNairita Pal,^{1,*} Susan Kurien,^{2,†} Timothy Clark,^{3,‡} Denis Aslangil,^{4,§} and Daniel Livescu^{5,||}¹*Applied Mathematics and Plasma Physics (T-5) and Center for Nonlinear Studies, Theoretical Division, Los Alamos National Laboratory, New Mexico 87545, USA*²*Applied Mathematics and Plasma Physics (T-5), Theoretical Division, Los Alamos National Laboratory, New Mexico 87545, USA*³*Department of Mechanical Engineering, University of New Mexico, Albuquerque New Mexico, New Mexico 87131, USA*⁴*Department of Mechanical Engineering and Mechanics, Lehigh University, Bethlehem, Pennsylvania 18015, USA*⁵*Los Alamos National Laboratory, Los Alamos, New Mexico 87545, USA*

(Received 12 July 2018; published 26 December 2018)

We present a study of buoyancy-driven variable-density homogeneous turbulence, using a two-point spectral closure model. We compute the time-evolution of the spectral distribution in wave number k of the correlation of density and specific volume $b(k)$, the velocity associated with the turbulent mass flux $\mathbf{a}(k)$, and the turbulent kinetic energy $E(k)$, using a set of coupled equations. Under the modeling assumptions, each dynamical variable has two coefficients governing spectral transfer among modes. In addition, the velocity $\mathbf{a}(k)$ has two coefficients governing the drag between the two fluids. Using a prescribed initial condition for $b(k)$ and starting from a quiescent flow, we first evaluate the relative importance of the different coefficients used to model this system and their impact on the statistical quantities. We next assess the accuracy of the model, relative to direct numerical simulation of the complete hydrodynamical equations, using b , \mathbf{a} , and E as metrics. We show that the model is able to capture the spectral distribution and global means of all three statistical quantities at both low and high Atwood number for a set of optimized coefficients. The optimization procedure also permits us to discern a minimal set of four coefficients which are sufficient to yield reasonable results while pointing to the mechanisms that dominate the mixing process in this problem.

DOI: [10.1103/PhysRevFluids.3.124608](https://doi.org/10.1103/PhysRevFluids.3.124608)**I. INTRODUCTION**

The mixing of fluids with different densities is an important process in many practical applications such as oceanic or atmospheric flows, combustion, and inertial confinement fusion. Variable-density flows are those in which fluctuations of the density from its mean value are large. To predict the effects of such large density fluctuations on the mean flow in complex systems, we require efficient computational models that are accurate, and also economical to run [1–3]. In the case of constant density turbulence there has been progress in model development [4,5].

*nairitap2009@gmail.com

†skurien@lanl.gov

‡ttc@unm.edu

§denis.aslangil@lanl.gov

||livescu@lanl.gov

There are well-known efforts in the literature on two-point (spectral) models for constant density, homogeneous isotropic turbulence in which energy transfer is described in wave number space using the eddy damped quasilinear closure introduced in Ref. [6], with further developments for homogeneous flows in Refs. [7,8]. In these efforts, the EDQNM framework is used to close the hierarchy arising due to the triadic interactions in the nonlinear term. More recently, there has been development in the studies of strongly anisotropic, homogeneous flow, with unstably stratified homogeneous turbulence (USHT) [9], and for shear-driven and buoyancy-driven turbulent flows [10], both of which have been computed using anisotropic EDQNM first developed in Ref. [8]. Spectral models of buoyancy-driven flows have been studied in Refs. [11,12] for the USHT system. The modeling of anisotropic contributions in homogeneous turbulence has been largely addressed in Refs. [10,13–15]. A novel approach to model the anisotropic contributions using the spherical harmonic decomposition has been undertaken in Refs. [16,17]. Two-point closures using EDQNM has been applied to inhomogeneous turbulence in Refs. [18,19]. Nonstationary inhomogeneous turbulence using the shear-free mixing layer has been studied using the two-point spectral closure model developed for the purpose [20,21].

It may be observed that in the above works, the approach has been to capture increasing degrees of complexity in the flow, ranging from homogeneous and isotropic, to inhomogeneous and anisotropic. Furthermore, the common factor in much of previous work has been they have largely considered single-fluid, incompressible flows. We, on the other hand, are interested in mixing between two fluids in the variable-density regime. Variable-density flows pose a difficulty beyond those encountered in incompressible single-fluid systems; the divergence-free condition of the velocity is lost and a pressure-strain correlation becomes nontrivial. Additional variables are introduced due to the coupling between the fluids and the driving mechanism. Variable-density flows have been studied in experiments [22–24], or using direct numerical simulations [25,26]. However, analytical models for such flows are mainly limited to single-point closure models [27–30], in which turbulence variables are studied as a function of a single space point. The latter suffer the drawback of being incapable of capturing transients and scale generation [31], a fundamental feature of turbulence.

In this paper, we work with a two-point spectral closure model for constant-density turbulent flow originally developed in Ref. [20], and modified in Refs. [32,33] for variable-density flows. The advantage of a model based on two-point correlations is its ability to capture the evolution of scales with time. As a result, one does not need to specify an extra equation for the dissipation as is needed in one-point models [2,34]. Our work bears some resemblance to Ref. [35], although that work is focused only on the kinetic energy evolution. In our work, the initial condition is specified by the two-point correlation of density fluctuation with specific-volume fluctuation defined as a distribution in wave number space. This quantity $b(k)$ in turn drives a velocity associated with the turbulent mass flux $\mathbf{a}(k)$, defined as the two-point correlation of the turbulent momentum with the specific volume, through a modulation of the pressure gradient. Consequently this turbulent flux velocity drives the generation of Reynolds stress and conversion of potential energy into turbulent kinetic energy $E(k)$. This coupled system is spatially homogeneous, which allows us to isolate the variable-density component of the model without the complications that may have been introduced by, say, inhomogeneity as in the classical inhomogeneous Rayleigh-Taylor (RT) problem. It must be noted, that our test problem is indeed the RT instability problem, posed in a manner that homogenizes it in space. A recent work which explores USHT (comparable to homogeneous RT instability) has been undertaken in Ref. [9] and is a detailed study of modeling the anisotropy in the flow using truncated expansions of correlation function in the basis of spherical harmonics. The critical departure from the approach in Ref. [9] occurs at the outset in that our flow of interest is non-Boussinesq, and we primarily focus on assessing the variable-density effects. We do not account for anisotropy explicitly apart from showing *a posteriori* that the model recovers the test data behavior satisfactorily even with the isotropic assumption. Some of the authors of the present work have considered anisotropic effects extensively both in rapid distortion limits and in terms of general solutions of the equations

of motion [16,17]. Nevertheless for the present study with its focus on mixing, the investigation of contributions due to anisotropy is mostly left for future work.

The closure assumptions for the spectral model truncate the hierarchy of equations at the level of the triple-correlations. For the variable-density case, this introduces two coefficients for each dynamical variable, expressing nonlinear spectral transfer. Additionally, a spectral drag governing the breakup of fluid elements in scale is introduced following Ref. [36], giving rise to two more coefficients in the evolution of \mathbf{a} .

In the first part of our study, for a prescribed artificial initial $b(k)$ following Ref. [37] we show how these coefficients affect the time evolution of the integrated model variables. The spectral transfer coefficients are varied pairwise for each evolution equation while keeping all other constants fixed to their nominal values specified by benchmark studies in Refs. [29,32,37]. We then determine suitable constants by comparison against direct numerical simulations (DNSs) of the system described in Refs. [26,38], following an optimization procedure. With these optimized constants, we find that the time evolution of the integrated mixing parameter b and velocity \mathbf{a} are well represented by the model. The integrated turbulent kinetic energy E is qualitatively well captured including the timing of the peak but shows some deficits in the magnitude of the peak.

II. MODEL EQUATIONS AND IMPLEMENTATION

We will follow the development proposed for single-fluid incompressible flow by Besnard *et al.* [20] and subsequently adapted for variable-density flow by Refs. [32,33]. We first decompose the flow field variables, i.e., density ρ , velocity \mathbf{u} , and pressure p into their mean and fluctuating parts as follows:

$$\rho = \bar{\rho} + \rho', \quad (1)$$

$$\mathbf{u} = \bar{\mathbf{u}} + \mathbf{u}', \quad (2)$$

$$p = \bar{p} + p', \quad (3)$$

where the overbar denotes the mean, and the primes the fluctuations about the mean. In the case of variable-density flows, it is useful to work with the mass-weighted averages introduced by Favre, known as Favre averages. So the Favre-averaged velocity $\tilde{\mathbf{u}}$ is

$$\tilde{\mathbf{u}} = \frac{\overline{\rho\mathbf{u}}}{\bar{\rho}}. \quad (4)$$

Let \mathbf{u}'' denote the fluctuation about this Favre averaged velocity $\tilde{\mathbf{u}}$. Then we have

$$\mathbf{u} = \tilde{\mathbf{u}} + \mathbf{u}''. \quad (5)$$

If we apply the standard Reynolds decomposition to $\overline{\rho\mathbf{u}}$ we get

$$\overline{\rho\mathbf{u}} = \bar{\rho}\bar{\mathbf{u}} + \overline{\rho'\mathbf{u}'} \quad (6)$$

since $\overline{\mathbf{u}'} = 0$ and $\overline{\rho'} = 0$. Using Eq. (4) we then obtain

$$\bar{\rho}\tilde{\mathbf{u}} = \bar{\rho}\bar{\mathbf{u}} + \overline{\rho'\mathbf{u}'}, \quad \tilde{\mathbf{u}} = \bar{\mathbf{u}} + \frac{\overline{\rho'\mathbf{u}'}}{\bar{\rho}}. \quad (7)$$

We define a velocity \mathbf{a} associated with the net turbulent mass flux as

$$\mathbf{a} = \frac{\overline{\rho'\mathbf{u}'}}{\bar{\rho}}. \quad (8)$$

From Eq. (7) then, we can define \mathbf{a} as the flux of mass relative to $\tilde{\mathbf{u}}$.

For two arbitrary points \mathbf{x}_1 and \mathbf{x}_2 in space, the mass-weighted Reynolds stress tensor is defined as

$$R_{ij}(\mathbf{x}_1, \mathbf{x}_2) = \frac{1}{2} \overline{[\rho(\mathbf{x}_1) + \rho(\mathbf{x}_2)] u_i''(\mathbf{x}_1) u_j''(\mathbf{x}_2)}, \quad (9)$$

the velocity associated with the turbulent mass flux is defined as

$$a_i(\mathbf{x}_1, \mathbf{x}_2) = -\overline{u_i''(\mathbf{x}_1) \rho(\mathbf{x}_1) v(\mathbf{x}_2)}, \quad (10)$$

and the covariance of the density and specific volume is defined as

$$b(\mathbf{x}_1, \mathbf{x}_2) = -\overline{\rho'(\mathbf{x}_1) v'(\mathbf{x}_2)}. \quad (11)$$

Subscripts i and j indicate Cartesian components, the specific volume is $v(\mathbf{x}) = \frac{1}{\rho(\mathbf{x})}$, and its fluctuations $v'(\mathbf{x})$ are defined with respect to the mean specific volume. The Favre averaging is a choice made both due to the history of this particular model and because it renders the energy equation in conservative form. In Ref. [9] the Boussinesq case does not employ any special density weighted averaging, but analogies may be drawn between their variable and these up to the normalization by density. Our b variable corresponds in that case to the two-point correlation of density fluctuation and is therefore analogous to potential energy.

The model is further developed in spectral space for which we require Fourier transformed variables. It is useful to rewrite the arguments in terms of position $\mathbf{x} = \frac{1}{2}(\mathbf{x}_1 + \mathbf{x}_2)$ and scale $\mathbf{r} = \mathbf{x}_1 - \mathbf{x}_2$ and Fourier transform so that \mathbf{k} is the wave vector associated with scale \mathbf{r} , so that

$$R_{ij}(\mathbf{x}, \mathbf{k}) = \int R_{ij}(\mathbf{x}, \mathbf{r}) e^{-i\mathbf{k}\cdot\mathbf{r}} d\mathbf{r}, \quad (12)$$

$$a_i(\mathbf{x}, \mathbf{k}) = \int a_i(\mathbf{x}, \mathbf{r}) e^{-i\mathbf{k}\cdot\mathbf{r}} d\mathbf{r}, \quad (13)$$

$$b(\mathbf{x}, \mathbf{k}) = \int b(\mathbf{x}, \mathbf{r}) e^{-i\mathbf{k}\cdot\mathbf{r}} d\mathbf{r}. \quad (14)$$

To simplify further, we average over the sphere in \mathbf{k} -space to obtain

$$R_{ij}(\mathbf{x}, k) = \int R_{ij}(\mathbf{x}, \mathbf{k}) \frac{k^2 d\Omega_k}{4\pi}, \quad (15)$$

$$a_i(\mathbf{x}, k) = \int a_i(\mathbf{x}, \mathbf{k}) \frac{k^2 d\Omega_k}{4\pi}, \quad (16)$$

$$b(\mathbf{x}, k) = \int b(\mathbf{x}, \mathbf{k}) \frac{k^2 d\Omega_k}{4\pi}, \quad (17)$$

where $d\Omega_k = \sin\theta d\theta d\phi$ for $0 \leq \theta \leq \pi$, $0 \leq \phi \leq 2\pi$. Henceforth we will use R_{ij} , a_i , and b to denote the spectral quantities at a certain time t and will drop their respective arguments. We will explicitly state their arguments when the variables are functions of time t only. Following Steinkamp *et al.* [32] we write the mass and momentum conservation equations for variable-density flows driven by gravity in the y direction as follows:

$$\frac{\partial \bar{\rho}}{\partial t} + \frac{\partial \bar{\rho} \tilde{u}_y}{\partial y} = 0, \quad (18)$$

$$\frac{\partial \bar{\rho} \tilde{u}_y}{\partial t} + \frac{\partial \bar{\rho} \tilde{u}_y \tilde{u}_y}{\partial y} = -\frac{\partial \bar{p}}{\partial y} + \bar{\rho} g - \frac{\partial R_{yy}}{\partial y}. \quad (19)$$

If we write the equations for the fluctuating density and velocity fields, and take the proper convolutions [20,37], we obtain the evolution equations for the Reynolds stress R_{ij} , velocity a_i , and the covariance of the density and specific volume b . These equations contain triple correlations of the velocity and density fluctuations which represent the turbulence cascade in k -space. Based on

the diffusion approximation model proposed by Leith [39], we model these triple correlation terms as nonlinear advection and diffusion in k -space [20,37,39]. We modify Steinkamp's set of equations for statistically homogeneous variable-density flow, keeping the gravity direction the same, and arrive at the following set of equations [32,33]:

$$\frac{\partial R_{nn}}{\partial t} = 2a_y \frac{\partial \bar{p}}{\partial y} + \frac{\partial}{\partial k} \left[k \Theta^{-1} \left(-C_{r1} R_{nn} + C_{r2} k \frac{\partial R_{nn}}{\partial k} \right) \right] - 2\nu k^2 R_{nn}, \quad (20)$$

$$\begin{aligned} \frac{\partial a_y}{\partial t} = & \frac{b}{\bar{\rho}} \frac{\partial \bar{p}}{\partial y} - (C_{rp1} k^2 \sqrt{a_{\hat{n}} a_{\hat{n}}} + C_{rp2} \Theta^{-1}) a_y \\ & + \frac{\partial}{\partial k} \left[k \Theta^{-1} \left(-C_{a1} a_y + C_{a2} k \frac{\partial a_y}{\partial k} \right) \right] - (\nu + \kappa) k^2 a_y, \end{aligned} \quad (21)$$

$$\frac{\partial b}{\partial t} = \frac{\partial}{\partial k} \left[k \Theta^{-1} \left(-C_{b1} b + C_{b2} k \frac{\partial b}{\partial k} \right) \right] - 2\kappa k^2 b, \quad (22)$$

where the turbulence frequency $\Theta^{-1} = \sqrt{\int_0^{k_1} \frac{k^2 R_{nn}}{\bar{\rho}} dk}$. In Eqs. (20)–(22) the dynamical variables R_{nn} , a_y , and b , respectively, are functions of k . The equations in Ref. [32] have been modified to introduce viscosity and diffusion terms necessary for comparison with DNS studies. In the original papers by Steinkamp there was an additional equation for the vertical component of Reynolds stress, R_{yy} , since that was an inhomogeneous system in which R_{yy} coupled directly back into both the velocity associated with the mass flux and the energy. In our homogeneous system this mechanism is absent, and it is therefore safe to omit that equation. Equations (18) and (19) are the mass and momentum conservation laws, respectively. The first term on the right-hand side (RHS) of Eq. (22) is based on a model proposed by Leith [39] for a nonlocal integral cascade with a wavelike part (the C_{b1} term) and a diffusive part (the C_{b2} term). Note that, if we retain the C_{b1} term only in the RHS, it will produce a wave equation (a hyperbolic equation) on taking a second derivative of b with respect to time. Hence the C_{b1} term, which is also the advection of b in k -space is “wavelike.” For $C_{b1} > 0$, the wavelike cascade of b is always forward (i.e., towards higher wave numbers), and $C_{b2} > 0$ results in a forward as well as inverse cascade [32]. The cascade terms for R_{nn} and a_y in Eqs. (20) and (21), respectively, are written in an analogous manner [32]. The drag between the fluids is described in the mass-flux equation (21) by the second term on the RHS. Here $a_{\hat{n}}$ is the component of \mathbf{a} normal to the fluid interface. The C_{rp1} term represents a drag arising between interpenetrating fluids at different scales [37,40,41]. The C_{rp2} term represents conventional drag governed by the turbulence timescale [37]. Previous spectral models ([32,33]) neglected explicitly the viscous and diffusive effects, while our aim here is to build a model for turbulence with viscous dissipation. Therefore we had dissipation terms proportional to the diffusion coefficient κ and the kinematic viscosity coefficient ν . We assume a Schmidt number $Sc = \nu/\kappa = 1$. We assume that the diffusion of $b(k)$ occurs in the manner of passive scalar diffusion [42].

Since we are implementing a system which is homogeneous, only k -dependent terms appear in the equations. This allows us to use only one cell for the physical direction in the computational domain. The pressure gradient term $\frac{\partial \bar{p}}{\partial y}$ term in the gravity direction is independent of y . We calculate $\frac{\partial \bar{p}}{\partial y}$ directly from Eq. (19) as

$$\frac{\partial \bar{p}}{\partial y} = \frac{g + \int_0^\infty (C_{rp1} k^2 \sqrt{a_{\hat{n}} a_{\hat{n}}} + C_{rp2} \Theta^{-1} + 2\nu k^2) a_y(k) dk}{\frac{1 + \int_0^\infty b(k) dk}{\bar{\rho}}}. \quad (23)$$

The spectral model calculations presented in this paper are performed with a code using a second-order MacCormack scheme [43] for time integration. This code is a modified version of a code used previously for studying variable-density mixing in the RT configuration [32,33]. For the purposes of code verification we also compare our results against an independent code which uses a

second-order Crank-Nicolson [44] scheme for time advancement. In this way we can assess confidence in the accuracy of our codes. The latter code is used only for verification. The results presented are based on the code using the second-order MacCormack scheme for time advancement. Both computer codes use an exponential grid for the wave number

$$k = k_s \exp \left\{ \frac{z}{z_s} \right\},$$

where k_s and z_s are scale factors and assumed to be equal to unity [20]. The variables computed are, in fact, kR_{nn} , kR_{ij} , ka_i , and kb . This choice of variables results in the cascade terms retaining a conservation form when expressed in terms of z rather than k . Likewise, the values of the integrals of the spectral quantities are easily determined, e.g.,

$$R_{nn}(t) = \int_0^{+\infty} R_{nn}(k, t) dk = \int_{-\infty}^{+\infty} R_{nn}(z, t) \frac{k_s}{z_s} \exp \left\{ \frac{z}{z_s} \right\} dz. \quad (24)$$

Setting $k_s = 1$ and z_s gives

$$R_{nn}(t) = \int_{-\infty}^{+\infty} \exp(z) R_{nn}(z, t) dz,$$

where $\exp(z)R_{nn}(z, t) = kR_{nn}(k, t)$. The explicit MacCormack methodology is nominally second-order accurate in time and space and utilizes two steps. Each of the two steps uses single-sided differences for the first-order derivatives, and the sides at which the differences are evaluated are different for the two steps, i.e., the left side for the first step and right side for the second. The second code utilizes a Crank-Nicolson method for time advancement and central differences for the z -space derivatives. The implicit evaluations of the cascades are decoupled for the various variables. However, the implicit step of the Crank-Nicolson method is iterated to achieve a coupling between the variables and to bring the nonlinear terms, i.e., the turbulent frequency term Θ^{-1} , up to date. This typically requires three or four iterations to converge. The implicit cascade is solved using a tridiagonal solver. The code is thus second-order accurate in time and space and unconditionally stable at all time steps. It should be noted that large time steps may necessitate more iterations to converge.

The boundary conditions at $k = 1$ and $k = k_{\max}$ are set to Neumann (zero flux). We initialize our model calculations with spectra for b , a_y , and R_{nn} at initial time $t = t_0$. We provide a value for the average density which corresponds to $\frac{\rho_{\max} + \rho_{\min}}{2}$ (here ρ_{\max} is the maximum density and ρ_{\min} is the minimum density in the variable-density fluid mixture). The spectral code requires the information of the mean density, and the details of the density contrast between the fluids are present only in the initial spectral distribution of b , a_y , and E .

In presenting results we will use integrated quantities as well as spectra for analysis. The integrated quantities are $b(t) = \int b(k, t) dk$, $a(t) = \int a_y(k, t) dk$, and $R_{nn}(t) = \int R_{nn}(k, t) dk$. $R_{nn}(t)$ is related to the turbulent kinetic energy $E(t)$ in the following way:

$$E(t) = \frac{1}{2\bar{\rho}} R_{nn}(t). \quad (25)$$

The set of equations (20)–(22) can describe a wide variety of homogeneous variable-density flows. We will focus on two canonical types of flow. The first is described by a nonzero initial distribution of $b(k)$ [37] with other variables set to zero and will be used to benchmark the calculations against previous efforts. The second type of flow is that computed in Refs. [26,38] and is initialized by $b(k)$ describing a distribution of blobs of one fluid in another with both a_y and R_{ij} set to nominally small values. The latter choice is made so that the flow reaches a turbulent state in a reasonable period of (wall clock) time. These are discussed in the next section.

TABLE I. Nominal values of all coefficients and other model parameters in the code-testing phase as prescribed in Ref. [37].

C_{b1}	C_{b2}	C_{a1}	C_{a2}	C_{r1}	C_{r2}	C_{rp1}	C_{rp2}	ν	κ	k_{\max}
0.12	0.06	0.12	0.06	0.12	0.06	1.0	1.0	10^{-4}	10^{-4}	512

III. RESULTS

In this section, we present our main results, which can be broadly divided into three categories. First, we present studies to check the numerics of our variable-density model implementation. We compare the results from the model calculations performed using two codes which use different schemes for time advancement. We also demonstrate convergence with respect to grid refinement. Second, we show how the system parameters affect the time evolution of the variables under study, $a(t)$, $b(t)$, $E(t)$, for a test initial condition described by the $b(k)$ spectrum used in Ref. [37], and discuss the varying trends. Third, from this study of parameters, we choose an optimum set which minimizes error with respect to the outcomes of a highly resolved low Atwood number (the Atwood number is defined as $\frac{\rho_{\max} - \rho_{\min}}{\rho_{\max} + \rho_{\min}}$) DNS study of variable-density buoyancy-driven turbulence [45]. We use the same set of coefficients for a high Atwood number system and show that the time evolution of $b(t)$ and $a(t)$ are well captured, while there is less fidelity to $E(t)$. Overall, however, the same coefficients appear to reasonably capture the multiple stages of the mixing for a broad spread in Atwood number.

A. Code convergence and time-stepping accuracy

To begin, we test whether the spectral model code converges under different system resolutions. We choose an analytical form $b(k) = B_0 e^{-k^2}$, with $a_y(k) = E(k) = 0$ as our initial condition. Here B_0 is such that $\int_0^{k_{\max}} b(k) dk = 1$ at $t = 0$, where k_{\max} is the maximum number of k modes, and t is the time. The coefficient values used in this part of the study are listed in Table I. In Fig. 1 we show that the results converge as the grid in k -space is refined for a fixed vertical system size of 2π . As the resolution is increased from 256 to 1024 k -modes, both the global energy and the spectral distributions converge.

Next we compare our results for $k_{\max} = 256$ against those from a code using a Crank-Nicolson scheme for time integration for the same resolution. The results are shown in Figs. 2(a)–2(c) and demonstrate that errors due to the time-advancement scheme are not significant.

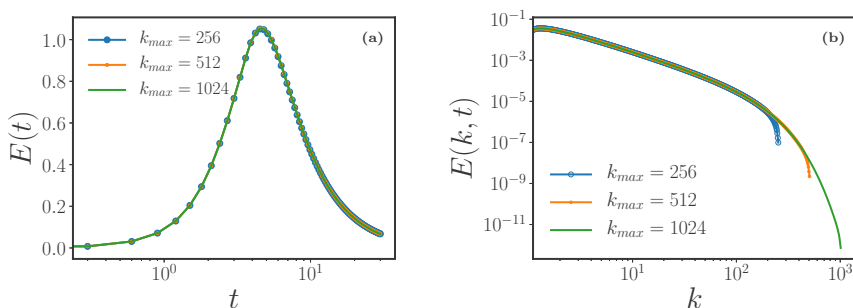


FIG. 1. Convergence of outcomes at increasing resolution for initial Gaussian distribution for $b(k)$, and $a_y(k)$, $E(k)$ set to zero at fixed viscosity $\nu = 10^{-4}$. (a) Time evolution plots of the turbulent kinetic energy $E(t)$ at different system resolutions and (b) kinetic energy spectra at different resolutions.

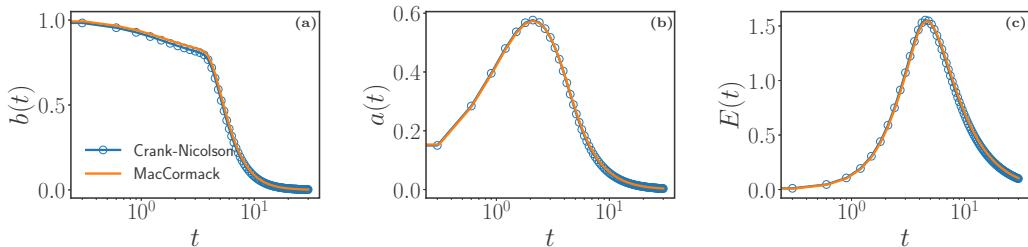


FIG. 2. Comparison of results from codes using Crank-Nicolson (blue line with circles) and MacCormack (orange line) schemes for time integration. Plots showing time evolution of (a) the mean density-specific volume covariance $b(t)$, (b) $a_y(t)$, and (c) the turbulent kinetic energy $E(t)$.

B. Coefficient variation study

There are eight coefficients in this model. The theoretical constraint for energy equipartition in the inviscid case $C_{r1} = 2C_{r2}$ [27,46] reduces the space to seven coefficients. Most of these arise from the closure approximation for the nonlinear (triple-correlation and higher-order) processes. The drag terms in the evolution of a_y were introduced in an *ad hoc* fashion [37] to provide an additional mechanism for the breakup of fluid structures in scale. The structure of the spectral transfer terms for b and a_y was originally written by analogy with the arguments provided in Ref. [20] for the energy spectral transfer. Given the rather nonrigorous quality of these arguments, but nevertheless taking the model at face value, it is worthwhile to assess what impact the systematic variation of these coefficients has on flow outcomes.

For the purposes of this study we systematically vary each coefficient while keeping the others fixed at their provisional values given in Ref. [37]. We then plot the integrated quantities $b(t)$, $a(t)$, and $E(t)$ as functions of time and describe how these vary relative to expected behaviors. In this test study, the same nonzero initial condition $b(k)$ as in the previous section provides the drive term for the velocity associated with the mass flux, which subsequently drives the growth of Reynolds stress R_{nn} . From Eq. (22) we note that the b equation has no production term in it, since there is no production of mass in the system. The sole contribution to $b(t)$ evolution is a redistribution in k -space via the terms weighted by coefficients C_{b1} and C_{b2} . Formally, based on the terms in the model, when C_{b1} is increased it should deplete $b(k)$ from the small k modes, i.e., the large length scales, and transfer them to the large k modes where they are dissipated by viscosity. This should increase the decay rate of $b(t)$ with time [Fig. 3(a)]. As $b(t)$ decays faster, peak of $a(t)$ is reduced, since there is less production of a_y (through the $\frac{b}{\rho} \frac{\partial \bar{p}}{\partial y}$ term). We see this is indeed the case in Fig. 3(b). The reduction in $a(t)$ reduces $E(t)$ because there is less production in R_{nn} (due to the $a_y \frac{\partial \bar{p}}{\partial y}$ term).

The coefficient C_{b2} multiplies a wavelike component and a diffusive component. Due to the wavelike part, an increase in C_{b2} would transfer $b(k)$ from the small k (large-scale) modes to the large k (small-scale) modes, and a diffusive transfer of $b(k)$ from the large k modes as well. Consistent with this interpretation, rate of decay of $b(t)$ becomes stronger as C_{b2} is increased, as shown in Fig. 4(d). Since b is coupled to a_y , there is a corresponding decrease in the peak of $a(t)$ as we increase C_{b2} [Fig. 4(e)] and a consequent reduction in the peak of $R_{nn}(t)$, and thus $E(t)$ [Fig. 4(f)].

In Eq. (21) for a_y , the spectral transfer part once again has two coefficients C_{a1} and C_{a2} . As C_{a1} is increased, more a_y should be transferred from small k to large k modes, where it is dissipated by viscosity. In Fig. 4(b) we see that increase in C_{a1} corresponds, as expected, to increasingly rapid decay of $a(t)$ in time as the spectral distribution terms become more important. Since a_y is coupled to R_{nn} through the pressure gradient term, $E(t)$ shows a dramatic decrease [Fig. 4(c)]. However, R_{nn} occurs in the inverse timescale Θ^{-1} . So, quite interestingly, reduction of R_{nn} reduces Θ^{-1} and thus slows the decay of $b(t)$ as we see from Fig. 4(a). C_{a2} affects the decay of $a(t)$ significantly, because increasing C_{a2} causes rapid transfer of a_y from intermediate k modes to large k modes, where they

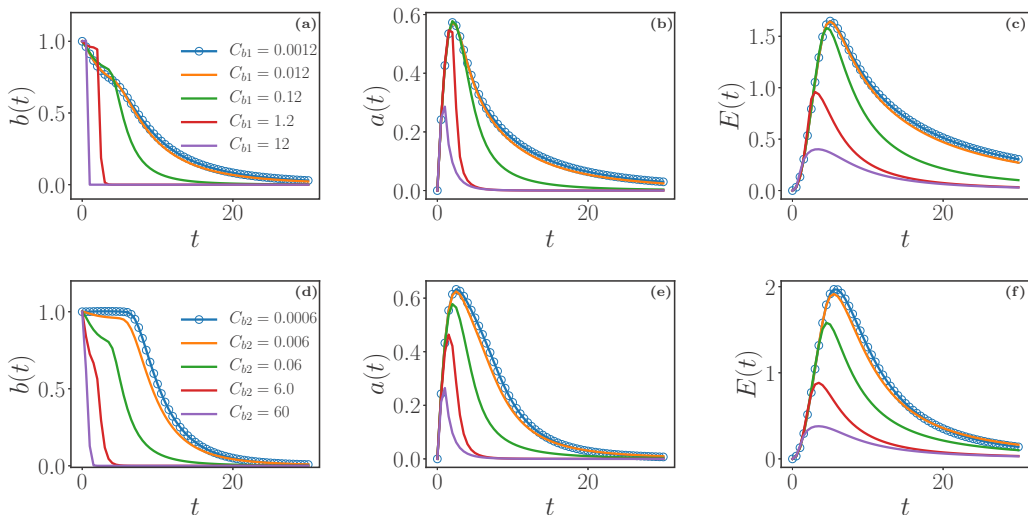


FIG. 3. Time evolution plots of (a) $b(t)$, (b) $a(t)$, and (c) $E(t)$ for different values of C_{b1} . Time evolution plots of (d) $b(t)$, (e) $a(t)$, and (f) $E(t)$ for different values of C_{b2} . The values of the parameters which do not vary in each case are shown in Table I. The number of k modes used is 512.

are dissipated due to the diffusive part in the spectral transfer term. So there is a substantial decrease in the peak of $a(t)$ [Fig. 4(e)] and the peak of $E(t)$ [Fig. 4(f)] as well. Reduction in R_{nm} results in a slower decay of $b(t)$ [Fig. 4(d)].

Next we vary the C_{r1} and C_{r2} coefficients pairwise, so as to maintain the condition $C_{r1} = 2C_{r2}$ [46]. When we increase C_{r1} and C_{r2} , the peak of the energy goes down, as well as the decay rates [Fig. 5(c)]. This results in a decrease if the inverse timescale Θ^{-1} . Thus $a(t)$ and $b(t)$ decay slowly [Figs. 5(a) and 5(b)]. It is interesting to note that the shape of the energy as a function of time is

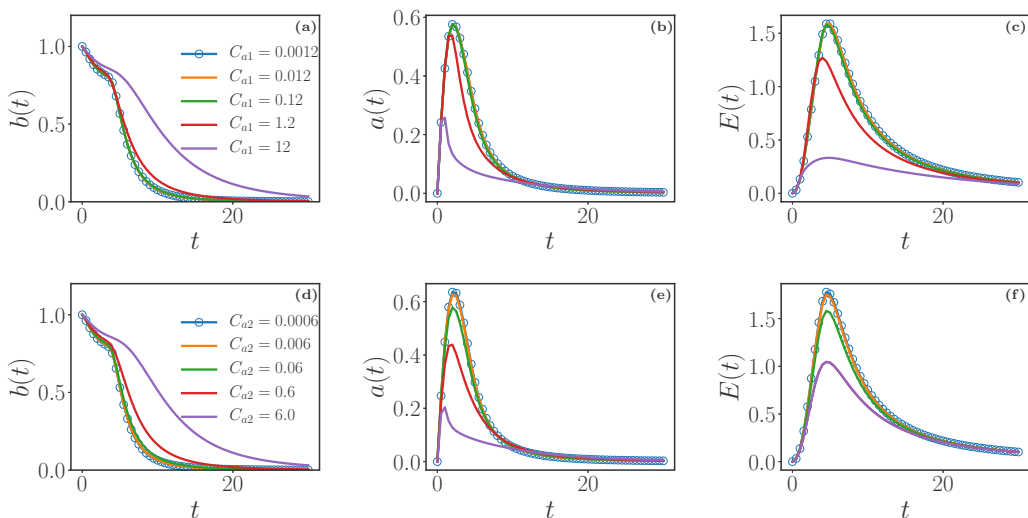


FIG. 4. Time evolution plots of (a) $b(t)$, (b) $a(t)$, and (c) $E(t)$ for different values of C_{a1} . Time evolution plots of (d) $b(t)$, (e) $a(t)$, and (f) $E(t)$ for different values of C_{a2} . The values of the parameters which do not vary in each case are shown in Table I.

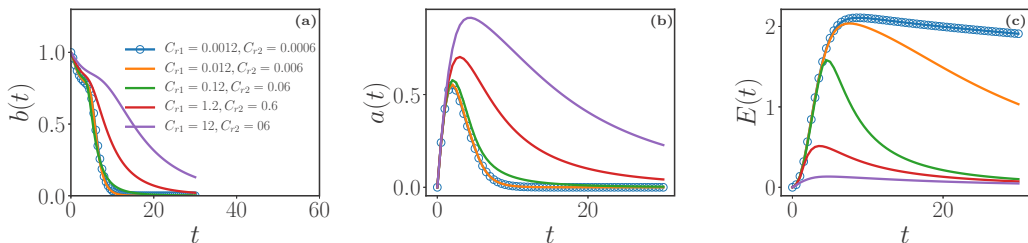


FIG. 5. Time evolution plots of (a) $b(t)$, (b) $a(t)$, and (c) $E(t)$ for different values of $C_{r1} = 2C_{r2}$. The values of the other parameters are shown in Table I.

very different for small values of the coefficients compared to the larger values. This variation study is the only one in our series that gives rise to this type of difference. However, it is consistent with the observation that as C_{r1} and C_{r2} go to zero the spectral redistribution of energy ceases and only the drive and dissipation terms remain. The inflected shape of the time series of energy as it decays [Fig. 5(c)] is thus captured only with proper information about spectral distribution.

We also look at the effects of varying the drag coefficients C_{rp1} and C_{rp2} on $b(t)$, $a(t)$, $E(t)$. As C_{rp1} is increased, drag on a_y increases, and thus the peak of $a(t)$ is suppressed [Fig. 6(b)]. This reduces the production of E , and thus the peak of $E(t)$ is also suppressed [Fig. 6(c)]. Reduction in E reduces the turbulence frequency Θ^{-1} . This slows the decay of $b(t)$ [Fig. 5(a)]. C_{rp2} increases the decay of $a(t)$ substantially [Fig. 5(e)], which in turn increases the decay of $E(t)$ [Fig. 5(f)]. This reduces the inverse timescale Θ^{-1} , which results in a slower decay rate for $b(t)$ [Fig. 5(d)].

These results are summarized in Table II for convenience. With some knowledge and intuition of the impact the model coefficients we next proceed to do a more in-depth study in comparison with DNS data of variable-density buoyancy-driven turbulence.

C. Comparison and optimization with respect to DNS data

In this section we will attempt to optimize the coefficients for a particular problem that has been exactly computed using the equations of motion in a highly resolved DNS. The goal is

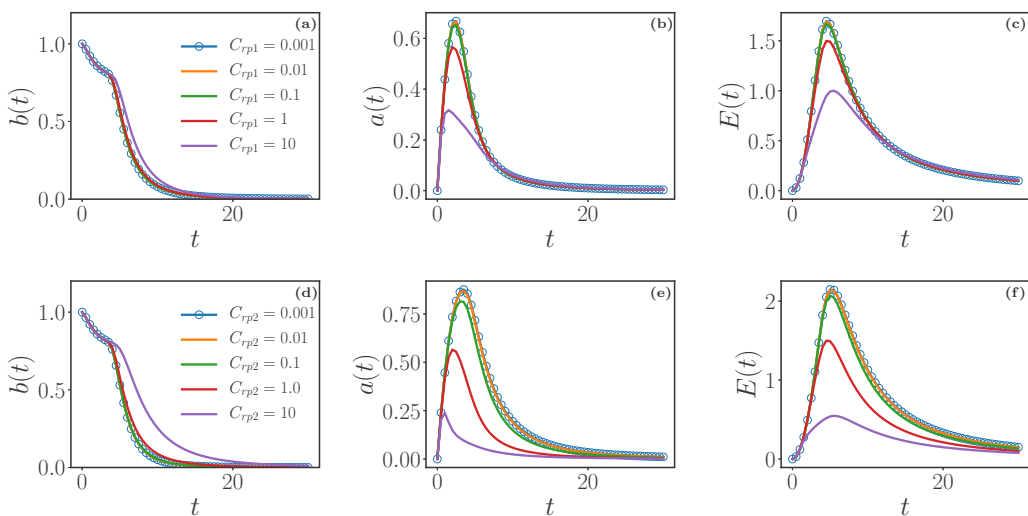


FIG. 6. Time evolution plots of (a) $b(t)$, (b) $a(t)$, and (c) $E(t)$ for different values of C_{rp1} . Time evolution plots of (d) $b(t)$, (e) $a(t)$, and (f) $E(t)$ for different values of C_{rp2} . The values of the parameters which do not vary in each case are shown in Table I.

TABLE II. The parameters C_{b1} , C_{b2} , C_{r1} , C_{r2} , C_{a1} , C_{a2} , C_{rp1} , and C_{rp2} for different calculations. The initial condition was a Gaussian in k -space for $b(k)$ field, and $a_y(k)$, $E(k)$ were set to zero. The system had 512- k modes. The viscosity is kept fixed at 10^{-4} . The diffusivity of the density field is also 10^{-4} .

	C_{b1}	C_{b2}	C_{r1}	C_{r2}	C_{a1}	C_{a2}	C_{rp1}	C_{rp2}	Effect
Effect on $b(t)$	0.0012–12	0.06	0.12	0.06	0.12	0.06	1.0	1.0	As C_{b1} increases, $b(t)$ decays faster
Effect on $a(t)$	0.0012–12.0	0.06	0.12	0.06	0.12	0.06	1.0	1.0	As C_{b1} increases, peak of $a(t)$ decreases
Effect on $R_{nm}(t)$	0.0012–12.0	0.06	0.12	0.06	0.12	0.06	1.0	1.0	As C_{b1} increases peak of $E(t)$ decreases
Effect on $b(t)$	0.12	0.006–6.0	0.12	0.06	0.12	0.06	1.0	1.0	Decay rate increases as C_{b2} increases
Effect on $a(t)$	0.12	0.006–6.0	0.12	0.06	0.12	0.06	1.0	1.0	Peak decreases as C_{b2} increases
Effect on $R_{nm}(t)$	0.12	0.006–6.0	0.12	0.06	0.12	0.06	1.0	1.0	Peak decreases as C_{b2} increases
Effect on $R_{nm}(t)$	0.12	0.06	0.0012–12.0	0.0006–6	0.12	0.06	1.0	1.0	As C_{r1} , C_{r2} increases, peak decreases
Effect on $a(t)$	0.12	0.06	0.0012–12.0	0.0006–6	0.12	0.06	1.0	1.0	As C_{r1} , C_{r2} increases, decay of $a(t)$ decreases
Effect on $b(t)$	0.12	0.06	0.0012–12.0	0.0006–6	0.12	0.06	1.0	1.0	As C_{r1} , C_{r2} increases, decay of $b(t)$ decreases
Effect on $a(t)$	0.12	0.06	0.12	0.06	0.0012–12	0.06	1.0	1.0	As C_{a1} increases, decay of $a(t)$ is better
Effect on $R_{nm}(t)$	0.12	0.06	0.12	0.06	0.0012–12.0	0.06	1.0	0.25	As C_{a1} increases, peak decreases
Effect on $b(t)$	0.12	0.06	0.12	0.06	0.0012–12.0	0.06	1.0	1.0	As C_{a1} increases, decay is slower
Effect on $a(t)$	0.12	0.06	0.12	0.06	0.12	0.006–6.0	1.0	1.0	Peak decreases as C_{a2} increases
Effect on $R_{nm}(t)$	0.12	0.06	0.12	0.06	0.12	0.006–6.0	1.0	1.0	Peak decreases as C_{a2} increases
Effect on $b(t)$	0.12	0.06	0.12	0.06	0.12	0.006–6.0	1.0	1.0	Decay rate decreases as C_{a2} increases
Effect on $a(t)$	0.12	0.06	0.12	0.06	0.12	0.06	0.0001–10.0	1.0	Peak decreases as C_{rp1} increases
Effect on $R_{nm}(t)$	0.12	0.06	0.12	0.06	0.12	0.06	0.0001–10.0	1.0	Peak decreases as C_{rp1} increases
Effect on $b(t)$	0.12	0.06	0.12	0.06	0.12	0.06	0.0001–10.0	1.0	Decay rate decreases as C_{rp1} increases
Effect on $a(t)$	0.12	0.06	0.12	0.06	0.12	0.06	1.0	0.0001–10	Peak decreases as C_{rp2} increases
Effect on $R_{nm}(t)$	0.12	0.06	0.12	0.06	0.12	0.06	1.0	0.0001–10	Peak decreases as C_{rp2} increases
Effect on $b(t)$	0.12	0.06	0.12	0.06	0.12	0.06	1.0	0.0001–10	Decay rate decreases as C_{rp2} increases

to demonstrate the operation of the model for a realistic problem and assess whether and how accurately the modeling assumptions capture both integrated and spectral quantities.

The DNS setup follows the triply periodic buoyancy-driven turbulence studied in Refs. [26,38]. This flow represents a homogeneous version of the classical RT instability and, during the growth

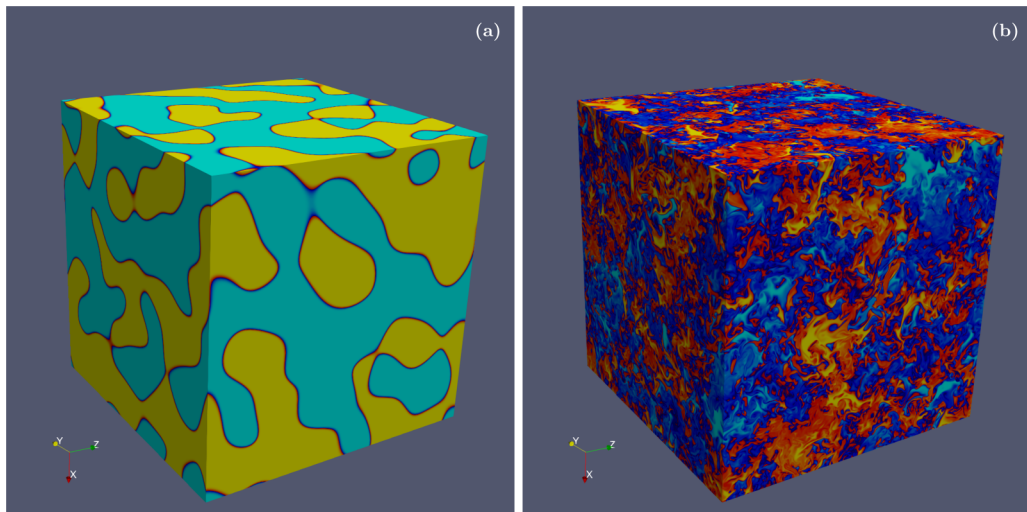


FIG. 7. 3D visualization of the density field for the $At = 0.05$ DNS run (1024^3 mesh) at (a) initial time and (b) turbulent kinetic energy peak time as described in Ref. [45].

stage, resembles the interior of the RT mixing layer. The flow is described by the variable-density Navier-Stokes equations, which are obtained as the incompressible (infinite speed of sound) limit of the fully compressible Navier-Stokes equations with two miscible species with different molar masses [47,48]. In this limit, the density variations arise from compositional changes as the two species mix and lead to nonzero divergence of velocity. The boundary conditions are triply periodic, and the two fluids are initialized as random blobs, consistent with the homogeneity assumption. The flow starts from rest, with only a small amount of dilatational velocity necessary to satisfy the divergence condition, and turbulence is generated as the two fluids start moving in opposite directions due to differential buoyancy forces. However, as the fluids become molecularly mixed, the buoyancy forces decrease and at some point turbulence start decaying. The nonstationary evolution of turbulence, resulting from the interplay between buoyancy turbulence production and mixing, is very difficult to be captured by one-point models [29].

To calibrate and test the spectral model, we use new higher resolution simulations [45]. Similar to Refs. [26,38], the simulations were performed with the CFDNS code [47] using a pseudospectral method. The time integration was performed with a third-order predictor-corrector Adams-Bashforth-Moulton method coupled with a pressure projection method, which results in a variable coefficient Poisson equation. The solution method uses direct Poisson solvers, with no loss of accuracy. The density contrast between the fluids is obtained from the value of the Atwood number $At = \frac{\rho_{\max} - \rho_{\min}}{\rho_{\max} + \rho_{\min}}$. Here we use two sets of simulations, with $At = 0.05$ and $At = 0.75$, on $(2\pi)^3$ domains discretized using 1024^3 meshes. The initial density spectrum is a top hat between wave numbers 3 and 5, resulting in a normalized initial density integral scale of 1.32 and a mixing state metric $\theta \sim 0.07$. The maximum turbulent Reynolds number attained by the two cases ($At = 0.05$ and $At = 0.75$) are 13 330 and 2230, resulting in Taylor Reynolds numbers using the isotropic formula of 298 and 122, respectively. Visualizations [Figs. 7(a) and 7(b)] of the density field at two different time points for $At = 0.05$ as obtained from the CFDNS code.

In order to remain as systematic as possible given the relatively large number of tuneable coefficients, we first assign nominal values prescribed in Refs. [32,37]. The values of $C_{r,1} = 0.12$ and $C_{r,2} = 0.06$, their relationship constrained in Ref. [46], have the most prior validation due to studies of single-fluid homogeneous isotropic and anisotropic flows [37,49]. Although we do not have a theoretical expectation for these in the variable-density case, the single fluid values

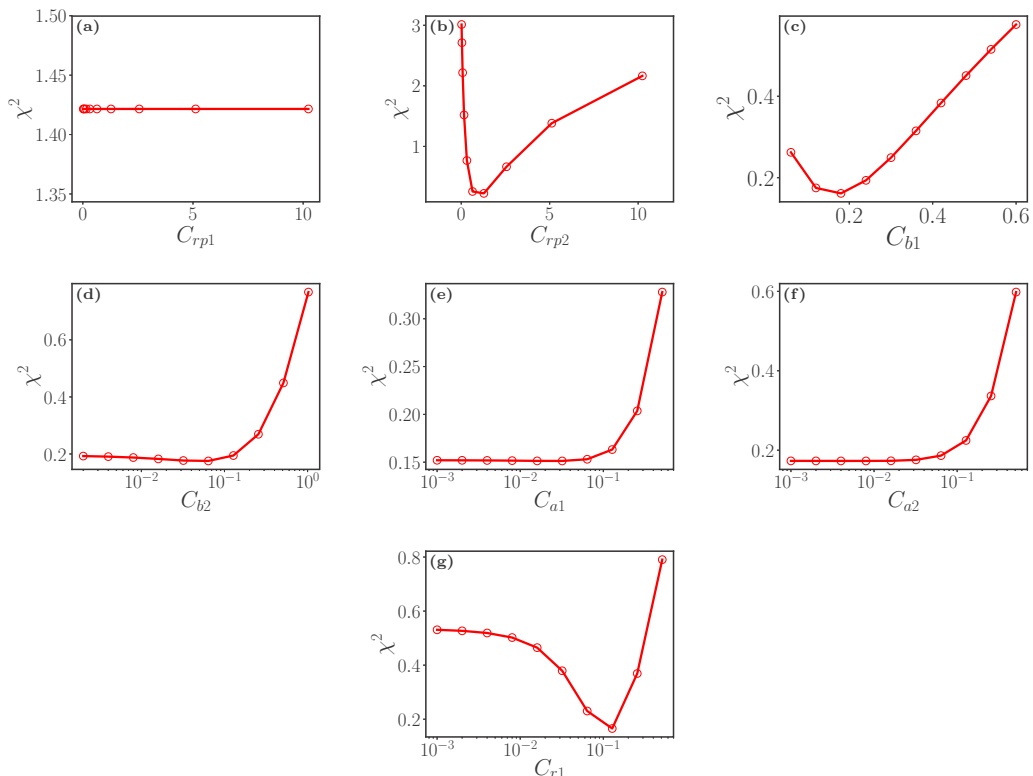


FIG. 8. Plots of χ^2 function calculated using Eq. (26) for different values of C_{rp1} , C_{rp2} , C_{b1} , C_{b2} , C_{a1} , C_{a2} , and C_{r1} . This minimum value of the χ^2 function occurs at the optimum value of each variable.

seem a reasonable place to search for an optimum. The corresponding spectral transfer coefficients for a (C_{a1} and C_{a2}) and b (C_{b1} and C_{b2}) were assigned to be identical to C_{r1} and C_{r2} , respectively, on a provisional basis in previous work, but there exists no theory or other expectation for these to the best of our knowledge. The drag coefficients for C_{rp1} and C_{rp2} were set to unity in Ref. [37] but assigned the values of 5 and 6, respectively, in Ref. [32] following arguments in Ref. [36] for effective drag around bluff bodies and spheres. We found that the values of 5 and 6 for C_{rp1} and C_{rp2} , respectively, in the present comparison were too high in that they strongly damped the growth of a relative to the DNS. Therefore we choose drag coefficients around unity as in Ref. [37].

We proceed to optimize the coefficients as follows. Each coefficient is varied, keeping all others fixed, and we can define the Pearson's χ^2 test function [50] as

$$\chi^2 = \sum_{t=0}^{t_{\max}} \frac{[(b_m - b_D) + (a_m - a_D)/a_0 + (E_m - E_D)/E_0]^2}{b_D + a_D/a_0 + E_D/E_0}, \quad (26)$$

where $b_m = b_m(t)$ refers to the mean density specific-volume correlation obtained from the model as a function of time, and $b_D = b_D(t)$ are the corresponding values from the resolved DNS. The quantities for a and E are defined analogously, and $a_0 = E_0 = 1$ are chosen so that they have the same dimensions as a_m and E_m , respectively. The upper limit on time $t_{\max} = 20$ in our case and is chosen so that the essential features of growth, peak, and decay are sufficiently captured without weighting the results too much by the very late times in which errors are naturally minimized.

We begin by optimizing the drag coefficient C_{rp1} keeping all other constants at their nominal values. Its optimum χ^2 value (and those of other coefficients subsequently) is found by minimizing the

TABLE III. Optimized values of all coefficients used for comparison with the DNS flow $At = 0.05$. Those values without uncertainties quoted correspond to χ^2 minima that asymptotically approach zero.

Parameter	C_{b1}	C_{b2}	C_{a1}	C_{a2}	C_{r1}	C_{r2}	C_{rp1}	C_{rp2}
R1	0.18 ± 0.06	0.05	0.12	0.06	0.12 ± 0.06	0.06	1.0	1.0 ± 0.5
R2	0.18 ± 0.06	0.0	0.0	0.0	0.12 ± 0.06	0.06	0.0	1.0 ± 0.5

function (26), as shown in the first panel of Fig. 8. As can be seen, the error function is relatively insensitive to variation in C_{rp1} , and retaining a value of unity is appropriate. The χ^2 as function of C_{rp2} shows a minimum at $C_{rp2} \sim 1.0$. We may prescribe a conservative uncertainty estimate on the minima by specifying (roughly) the range over which the minimum χ^2 is doubled. With this error specification, $C_{rp2} \simeq 1.0 \pm 0.5$ as is shown in Fig. 8(b), and so it is also retained as unity.

The other coefficients are optimized in a similar manner, and the quality of the optimizations are shown in Fig. 8. There are two types of minima observed for the χ^2 error functions shown. The first is a true parabolic minimum as for C_{rp2} , C_{b1} , and C_{r1} [Figs. 8(b), 8(c), and 8(g)], and the second is an asymptotic minimum as for C_{b2} , C_{a1} , and C_{a2} . The extreme case is the error with respect to the already discussed C_{rp1} , which shows no dependence of χ^2 on the coefficient value at all. Table III shows the optimized values (R1) of all coefficients for the $At = 0.05$ case along with their uncertainties. For the cases that do not have a clear minimum the nominal values from Ref. [37] are retained, and the range of uncertainty is taken to be all values between zero and the first instance of the minimum. Note that the values obtained by minimizing the error over all the dynamical variables simultaneously do not depart significantly from the nominal values proposed in Ref. [37]. Indeed, C_{r1} and C_{r2} , which may be derived from the Kolmogorov constant and the Lee equipartition constraint, are minimized at the theoretically expected values, which is a strong validation of the model and, less directly, of the assumption that the energy cascade in the variable-density mixing problem is not inconsistent with Kolmogorov dynamics.

Given the quality of the minima it is clear that the uncertainty in the coefficient choice may be quite large (between 30% and 50%) either because of the shallowness of the minima or the independence of the error function to values below a certain threshold. Due to the latter feature, we may be justified in taking the values of C_{rp1} , C_{rp2} , C_{b2} , C_{a1} , and C_{a2} to zero. The resulting sparse set of nonzero coefficients is denoted by R2 in Table III. This set represents an attempt to assess if a minimal number of coefficients may be extracted to yield a reasonable comparison with DNSs. Note that in both rows of values in Table III, those which do not have uncertainties quoted correspond to the coefficients with asymptotic minimum χ^2 .

In Figs. 9(a)–9(c) we show the comparison of the model calculations at the optimized parameters R1 (orange line) with the DNS data (blue line with circles). We observe reasonable agreement with

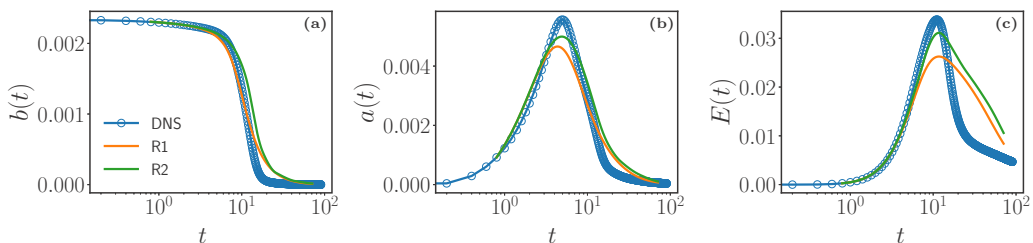


FIG. 9. Time evolution of flow with initial $At = 0.05$. (a) Mean density-specific volume covariance $b(t)$, (b) mean $a(t)$, and (c) turbulent kinetic energy $E(t)$ obtained from the results of the DNS calculations (blue line with circles) and from the spectral model [R1 (orange line) and R2 (green line)] with parameter values listed in Table III. DNS runs in this case are at a resolution of 1024^3 (the viscosity is 10^{-4}).

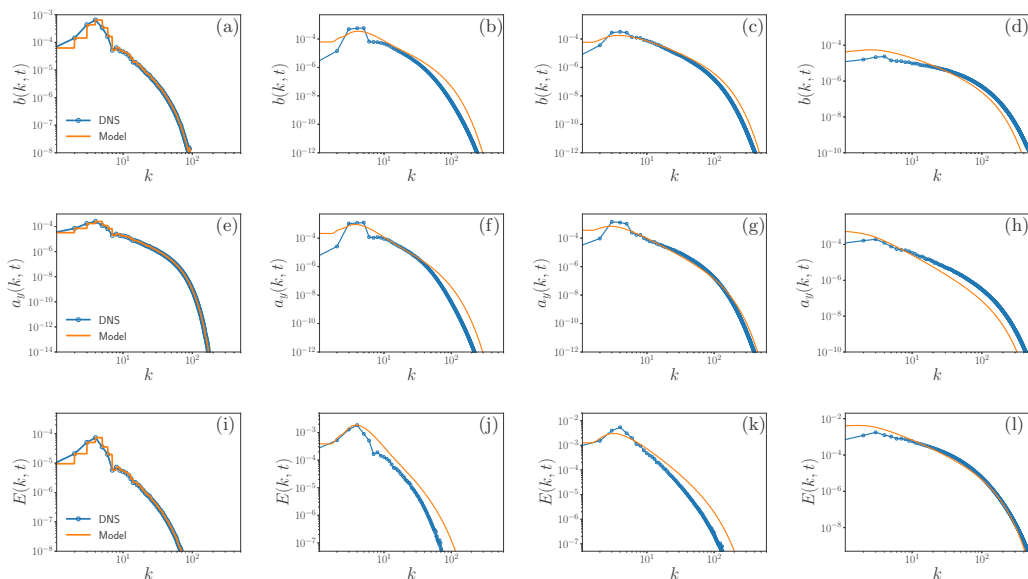


FIG. 10. Spectra of flows with initial $At = 0.05$. Plots of $b(k)$ versus the wave number k at times (a) $t = 0.8$, (b) $t = 3.2$, (c) $t = 6.4$, and (d) $t = 14$. $a_y(k)$ versus the wave number k at times (e) $t = 0.8$, (f) $t = 3.2$, (g) $t = 6.4$, and (h) $t = 14$. Energy $E(k)$ versus the wave number k at times (i) $t = 0.8$, (j) $t = 3.2$, (k) $t = 6.4$, and (l) $t = 14$. The parameters for these data are given in Table III with the corresponding DNS data resolution at 1024^3 .

the DNS data in the time evolution of $b(t)$ [Fig. 9(a)], $a(t)$ [see Fig. 9(b)], and the kinetic energy growth stage [see Fig. 9(c)]. The magnitude of the peak of the kinetic energy is underestimated by the model, although the timing of the peak is the same as that of the DNS. The decay of the kinetic energy computed by the spectral model is slower than the decay of the kinetic energy in the DNS. Overall the model has captured the global quantities quite well, especially given that our optimization function Eq. (26) requires no weighting of one quantity over another and is a fairly naive choice. All three primary regimes of the dynamics, namely, mix-driven growth of mass flux followed by conversion of potential energy to turbulent kinetic energy and subsequent decaying dynamics and a fully mixed state, are largely captured by the spectral model.

If we consider the minimal set of coefficients R2, we find that the comparison with DNS is very similar to that obtained by using the full set. Indeed the peak of $a(t)$ and energy are both in better agreement for R2. The decay regimes are more compromised in R2 as compared to R1. This procedure of minimization of an error function over all metrics is thus a way also to understand dominant processes and eliminate less critical contributions. Our analysis has shown that, of the modeled terms, the downscale transfer of b (governed by C_{b1}), the downscale and upscale redistribution of energy (governed by C_{r1} and C_{r2}), and the breakup of the scales of a due to turbulence (governed by C_{rp2}) are the dominant spectral processes. The exact terms for drive and dissipation are also important but clearly not sufficient. It is particularly interesting to note that the minimal set of coefficients also seems to imply that the spectral redistribution of a is entirely subdominant in the homogeneous variable-density mixing process. Our systematic study of the coefficients and a fairly simple optimization procedure has thus revealed useful constraints and properties both of the model as well as of the physical processes under study. These are a significant advantage in turbulence modeling.

We next show the spectral quantities computed by the optimized model for low At in Fig. 10. The first column shows the initial conditions of $b(k)$, $a_y(k)$, and $E(k)$ from the DNS in blue and the approximation used by the model in orange. By necessity, we use a coarse representation of

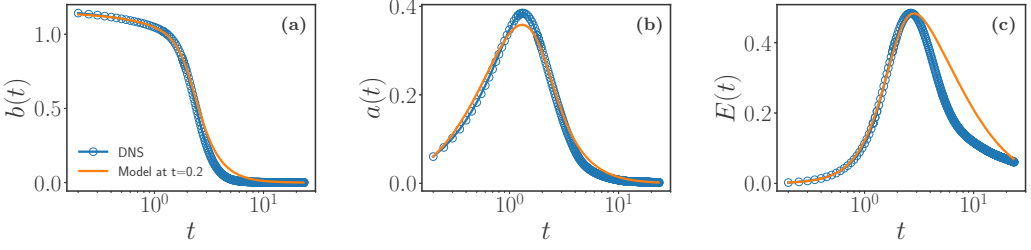


FIG. 11. Time evolution of flow with initial $At = 0.75$. (a) Mean density-specific volume covariance $b(t)$, (b) mean $a(t)$, and (c) turbulent kinetic energy $E(t)$ obtained from the results of the DNS calculations (blue line with circles) and from the spectral model code (orange line) with parameter values listed in Table III (run R1), and the corresponding DNS resolution is 1024^3 (the viscosity is 10^{-4}).

the spectra in the low wave numbers because of the implementation of the surrogate coordinate $z = z_s \ln(k/k_s)$ ($z_s = 1$ and $k_s = 1$). As time evolves the model spectra show good agreement with the DNS at the peak values (which dominate the integrals) but overpredict the spectra at both small and large k for intermediate time $t = 3.2$ (second column). As time evolves further to $t = 6.4$, both $a_y(k)$ and $b(k)$ model calculation show better agreement with DNS at higher k , but the high wave numbers for the energy remain overpredicted. The spectra thus permit a more detailed understanding of the flow dynamics than do the global quantities. Indeed we reiterate that our coefficient variation study demonstrated that spectral information was critical to developing the right time evolution [in Fig. 5(c), for example, very low values of the spectral transfer coefficients result in a substantially slow decay of E] particularly on the decay side of the process.

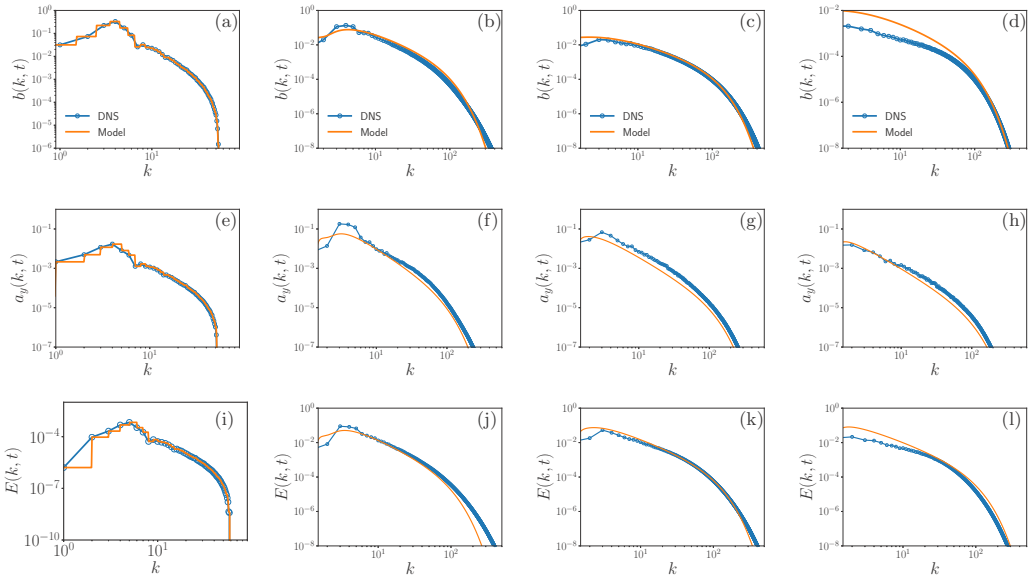


FIG. 12. Spectra of flows with initial $At = 0.75$. Plots of $b(k)$ versus the wave number k at times (a) $t = 0.2$, (b) $t = 1.8$, (c) $t = 3.0$, and (d) $t = 5.0$. $a_y(k)$ versus the wave number k at times (e) $t = 0.2$, (f) $t = 1.8$, (g) $t = 3.0$, (h) $t = 5.0$. Energy $E(k)$ versus the wave number k at times (i) $t = 0.2$, (j) $t = 1.8$, (k) $t = 3.0$, (l) $t = 5.0$. The parameters for these data are given in Table III with the corresponding DNS data resolution at 1024^3 .

For completeness we expand the discussion to a high Atwood number case $At = 0.75$. The Atwood number in the DNS was changed by increasing the density of the heavier fluid. This corresponds in the model to what we will call a “density contrast” since the Atwood number does not explicitly appear in the spectral model. This density contrast is implicit in the larger $\bar{\rho} = \frac{\rho_{\max} + \rho_{\min}}{2}$ that is specified in the model equations of motion. As a first attempt we use the coefficients optimized in the low Atwood number case shown in the R1 row in Table III. The results are shown in Fig. 11. We observe that the quantitative agreement with DNS is fairly good, similar to the low At case. Thus the optimization at low At also holds at high At. The decay of the kinetic energy is slow compared to the DNS [Fig. 11(c)]. Nevertheless, certain qualitative features are still captured quite well including the initial transition in $b(t)$ [Fig. 11(a)] and overall shape of $a(t)$ [Fig. 11(b)]. It must be noted that further iteration over the coefficients may well fine-tune the outcomes, but such an exercise lies beyond the scope of this paper.

We next show the spectral quantities for the high At in Fig. 12. Similar to Fig. 10 we plot the initial conditions of $b(k)$, $a_y(k)$, and $E(k)$, from the DNS and also the model in the first column. The subsequent plots of $a_y(k)$, $b(k)$, and $E(k)$ at times $t = 1.8$, $t = 3.0$, and $t = 5.0$ are shown in the second, third, and fourth columns, respectively. We note that the spectral evolution of $b(k)$, $a_y(k)$, and $E(k)$ are well captured with respect to the DNS data. Thus the spectral as well as the global quantities for high At show a good agreement with DNS data. This demonstrates that the spectral model is able to capture the different stages of variable-density flow evolution for different values of At with minimal change in system parameters.

IV. DISCUSSION AND CONCLUSION

We have benchmarked the two-point spectral model developed in Refs. [32,33,37] to study variable-density homogeneous turbulence. In summary we can observe some general trends. The main observation is that each dynamical variable is primarily affected by its spectral transfer terms governed by C_{V1} and C_{V2} (where V is any of b , a , or E). The direct effect is to reduce both peak value and delay the peak timing for the respective variable. However, the indirect effect on a coupled variable may be quite different. The most striking example of this is the response of the system to variation of C_{r1} and C_{r2} . Recall that the values of C_{r1} and C_{r2} were derived based on the Kolmogorov constant multiplying the spectrum and equipartition in the inviscid case. Therefore variation away from those values implicitly permits reinterpretation of the cascade processes in the model. In Fig. 5(c) the energy is reduced both in magnitude and in the decay rate. However, the indirect effect on $a(t)$ and $b(t)$, via the decrease in frequency Θ^{-1} and corresponding increase in characteristic turbulence timescale, results in delayed decay of both those quantities. Increasing this pair of variables is the only change that decreases energy while increasing both mass-flux velocity and the mixing parameter magnitude. This is a clear demonstration of how the turbulence timescale as implemented in the model operates as a governing parameter for the behavior of the dynamical variable.

The drag coefficients C_{rp1} and C_{rp2} for \mathbf{a} govern a different process than do the spectral transfer terms. The former have significant effect on $a(t)$ as expected and in turn on $E(t)$ because of the direct coupling via the pressure gradient. The mixing parameter $b(t)$ on the other hand is relatively insensitive to the drag on \mathbf{a} for low to moderate values of the drag coefficients. For very large values of those coefficients, the decay rate of $b(t)$ is slowed down. This may be understood in light of the fact that the drag on \mathbf{a} is a tertiary effect on b via the turbulence energy timescale Θ^{-1} . The processes governing the entire cycle of the flow may be completed before the timescale has the chance to grow enough to significantly impact $b(t)$.

In the second part of the study we test the model against DNS data. The purpose is to offer a spectral model for variable-density turbulence at high resolution with coefficients tuned to the problem and based on well-defined error parameters. We choose to optimize the coefficients on the low At case first and found that the model works well for the buoyancy production stage, as well as the decay of the different variables. In optimizing the coefficients we did not favor any one

dynamical variable over another; we could envision a more targeted application which, for example, specifies greater fidelity of the turbulent kinetic energy. In that case the fidelity to the mass-flux velocity and b will be compromised and a different set of coefficients deduced. Another important factor in the outcomes of the coefficients is the time over which the functions are optimized, in this case $0 < t \leq t_{\max} = 20$. If a different interval were chosen, one might do better at isolating, say, the growth phase or the decay phase. It is not our intention to provide a fixed set of coefficients but merely to demonstrate that the model can recover a realistic flow with satisfactory agreement to the global quantities and to the spectral distributions. Even with these caveats, it appears that several of the eight coefficients, and hence the processes corresponding to the terms that they multiply, become subdominant because of the manner in which they have asymptotically minimized errors for small values. The coefficients with true minima are C_{b1} , the downscale spectral transfer coefficient of b , C_{r1} and C_{r2} , both of which govern upscale and downscale spectral redistribution of turbulence kinetic energy, and C_{rp2} , which provides a mechanism for the breakup of fluid parcels in scale due to turbulence. It is important to note that C_{r1} and C_{r2} optimize to the values consistent with Kolmogorov and equipartition theory. This suggests that the cascade process in the variable-density mixing problem, at least from the point of view of a second-order spectral model, is consistent with that of the constant density Kolmogorov turbulence problem. It is worth mentioning here that the presence of density fluctuations may modify the nonlinear interactions and perhaps may not achieve equipartition in the case of large density fluctuations for the inviscid, nondiffusive truncated system. The choice of maintaining the $C_{r1} = 2C_{r2}$ for the energy cascade coefficients allows the energy cascade to be maintained in the constant density limit. However, this limit (constant density) is irrelevant for the correlations a and b since they vanish in this limit. It is possible that the cascade coefficients in this simple model may be variables of, say, the Atwood number. However, we have not explored this issue and have not seen the utility of this added complication at this point.

This emergence of four dominant coefficients leads to the understanding that, apart from the drive terms and the dissipation which are treated exactly, the model expressions for downscale transfer of b , the break-up of fluid blobs as they sink under gravity and couple with the turbulence, and the resulting redistribution of E in spectral space are the main mechanisms at play in the homogeneous variable-density mixing problem. At the level of second-order two-point correlations, therefore, the model points to and helps elucidate the dominant physical mechanisms at play.

The set of coefficients in Table III obtained from analysis of the low At data appear to be less suitable for a high Atwood number system $At = 0.75$, particularly as they relate to the energy. However, the comparison is qualitatively quite good overall considering that we performed only a first-order process for determining coefficients in the low At case and the difference in At for the two cases is very large. There is no approximation or assumption in the model development that requires Boussinesq or near-Boussinesq (low Atwood number) conditions. Therefore it is perhaps not surprising that one set of coefficients works quite well over a broad range of At.

In summary, the spectral model we have studied is able to recover the statistical and spectral outcomes from nontrivial physical processes in a mixing problem, with minimal tuning of coefficients for two widely different Atwood number flows. The tuning procedure is systematic and may be used to narrow down the space of unknown coefficients, which is always an advantage in predictive modeling. In future work, we will try to develop a more general understanding of flows with different density ratios and will address the canonical inhomogeneous RT mixing problem.

ACKNOWLEDGMENTS

We thank an anonymous referee for providing suggestions which led to a substantial improvement in our paper. N.P., S.K., and T.C. were funded by the Mix and Burn project under the Physics and Engineering Models program of the DOE Advanced Simulation and Computing program. N.P. thanks Center for Nonlinear Studies (CNLS), LANL for support. Work at LANL was performed under the auspices of the U.S. DOE, Contract No. DE-AC52-06NA25396. The DNS results were obtained using computational resources provided by the Institutional Computing Program at Los

Alamos National Laboratory and the Argonne Leadership Computing Facility at Argonne National Laboratory through a 2017 ALCC Award. D.A. acknowledges financial support from Prof. Arindam Banerjee, Lehigh University, through the DOE/NNSA SSAA Program (Grant No. DE-NA0003195) and the U.S. National Science Foundation Early CAREER Program (Grant No. 1453056).

-
- [1] A. A. Townsend, *The Structure of Turbulent Shear Flow* (Cambridge University Press, Cambridge, 1980).
 - [2] D. C. Wilcox *et al.*, *Turbulence Modeling for CFD* (DCW Industries, La Canada, CA, 1993), Vol. 2.
 - [3] K. Hanjalić, Advanced turbulence closure models: A view of current status and future prospects, *Int. J. Heat Fluid Flow* **15**, 178 (1994).
 - [4] K. Hanjalic, B. E. Launder, and R. Schiestel, Multiple-time-scale concepts in turbulent transport modeling, *Turbul. Shear Flows* **2**, 36 (1980).
 - [5] S. B. Pope, On the relationship between stochastic Lagrangian models of turbulence and second-moment closures, *Phys. Fluids* **6**, 973 (1994).
 - [6] S. A. Orszag, Analytical theories of turbulence, *J. Fluid Mech.* **41**, 363 (1970).
 - [7] C. Cambon, Modélisation spectrale en turbulence homogène anisotrope, Ph.D. thesis, Claude Bernard University, Lyon, 1979.
 - [8] C. Cambon, D. Jeandel, and J. Mathieu, Spectral modeling of homogeneous non-isotropic turbulence, *J. Fluid Mech.* **104**, 247 (1981).
 - [9] A. Briard, M. Iyer, and T. Gomez, Anisotropic spectral modeling for unstably stratified homogeneous turbulence, *Phys. Rev. Fluids* **2**, 044604 (2017).
 - [10] C. Cambon, V. Mons, B.-J. Gréa, and R. Rubinstein, Anisotropic triadic closures for shear-driven and buoyancy-driven turbulent flows, *Comput. Fluids* **151**, 73 (2017).
 - [11] A. Burlot, B.-J. Gréa, F. S. Godeferd, C. Cambon, and J. Griffond, Spectral modeling of high Reynolds number unstably stratified homogeneous turbulence, *J. Fluid Mech.* **765**, 17 (2015).
 - [12] A. Burlot, B.-J. Gréa, F. S. Godeferd, C. Cambon, and O. Soulard, Large Reynolds number self-similar states of unstably stratified homogeneous turbulence, *Phys. Fluids* **27**, 065114 (2015).
 - [13] C. Cambon and B.-J. Gréa, The role of directionality on the structure and dynamics of strongly anisotropic turbulent flows, *J. Turbulence* **14**, 50 (2013).
 - [14] C. Cambon and R. Rubinstein, Anisotropic developments for homogeneous shear flows, *Phys. Fluids* **18**, 085106 (2006).
 - [15] R. Rubinstein, S. Kurien, and C. Cambon, Scalar and tensor spherical harmonics expansion of the velocity correlation in homogeneous anisotropic turbulence, *J. Turbulence* **16**, 1058 (2015).
 - [16] R. Rubinstein, T. T. Clark, and S. Kurien, Leith diffusion model for homogeneous anisotropic turbulence, *Comput. Fluids* **151**, 108 (2017).
 - [17] T. T. Clark, S. Kurien, and R. Rubinstein, Generation of anisotropy in turbulent flows subjected to rapid distortion, *Phys. Rev. E* **97**, 013112 (2018).
 - [18] J.-P. Bertoglio and D. Jeandel, A simplified spectral closure for inhomogeneous turbulence: application to the boundary layer, in *Turbulent Shear Flows 5*, edited by F. Durst, B. E. Launder, J. L. Lumley, F. W. Schmidt, and J. H. Whitelaw (Springer, Berlin, Heidelberg, 1987), pp. 19–30.
 - [19] J.-P. Bertoglio, Two-point closures and turbulence modeling, in *3rd International Symposium on Turbulence and Shear Flow Phenomena* (International Center, Sendai, Japan, 2003).
 - [20] D. C. Besnard, F. H. Harlow, R. M. Rauenzahn, and C. Zemach, Spectral transport model for turbulence, *Theor. Comput. Fluid Dyn.* **8**, 1 (1996).
 - [21] A. D. Bragg, S. Kurien, and T. T. Clark, Model of non-stationary, inhomogeneous turbulence, *Theor. Comput. Fluid Dyn.* **31**, 51 (2017).
 - [22] S. Gerashchenko and K. Prestridge, Density and velocity statistics in variable density turbulent mixing, *J. Turbulence* **16**, 1011 (2015).
 - [23] B. Akula and D. Ranjan, Dynamics of buoyancy-driven flows at moderately high Atwood numbers, *J. Fluid Mech.* **795**, 313 (2016).

- [24] J. J. Charonko and K. Prestidge, Variable-density mixing in turbulent jets with coflow, *J. Fluid Mech.* **825**, 887 (2017).
- [25] W. H. Cabot and A. W. Cook, Reynolds number effects on Rayleigh–Taylor instability with possible implications for type Ia supernovae, *Nat. Phys.* **2**, 562 (2006).
- [26] D. Livescu and J. R. Ristorcelli, Variable-density mixing in buoyancy-driven turbulence, *J. Fluid Mech.* **605**, 145 (2008).
- [27] D. Besnard and F. H. Harlow, Turbulence in two-field incompressible flow, NASA STI/Recon Technical Report No. 86 (1985).
- [28] A. Banerjee, R. A. Gore, and M. J. Andrews, Development and validation of a turbulent-mix model for variable-density and compressible flows, *Phys. Rev. E* **82**, 046309 (2010).
- [29] J. D. Schwarzkopf, D. Livescu, J. R. Baltzer, R. A. Gore, and JR Ristorcelli, A two-length scale turbulence model for single-phase multi-fluid mixing, *Flow Turbul. Combust.* **96**, 1 (2016).
- [30] S. E. Elghobashi and T. W. Abou-Arab, A two-equation turbulence model for two-phase flows, *Phys. Fluids* **26**, 931 (1983).
- [31] T. T. Clark, Two-point closures and statistical equilibrium, in *Modeling Complex Turbulent Flows*, edited by M. D. Salas, J. N. Hefner, and L. Sakell (Springer, Dordrecht, 1999), pp. 183–202.
- [32] M. J. Steinkamp, T. T. Clark, and F. H. Harlow, Two-point description of two-fluid turbulent mixing. I. Model formulation, *Int. J. Multiphase Flow* **25**, 599 (1999).
- [33] M. J. Steinkamp, T. T. Clark, and F. H. Harlow, Two-point description of two-fluid turbulent mixing. II. Numerical solutions and comparisons with experiments, *Int. J. Multiphase Flow* **25**, 639 (1999).
- [34] J. D. Schwarzkopf, D. Livescu, R. A. Gore, R. M. Rauen Zahn, and J. R. Ristorcelli, Application of a second-moment closure model to mixing processes involving multicomponent miscible fluids, *J. Turbulence* **12**(49), N49 (2011).
- [35] D. Dupuy, A. Toutant, and F. Bataille, Equations of energy exchanges in variable density turbulent flows, *Phys. Lett. A* **382**, 327 (2018).
- [36] D. L. Youngs, A two-dimensional turbulence model based on the equations of multiphase flow, 3rd Zababahin Scientific Talks, Kishtim, USSR (1992).
- [37] T. T. Clark and P. B. Spitz, Two-point correlation equations for variable density turbulence, Technical Report, Los Alamos National Laboratory (1995).
- [38] D. Livescu and J. R. Ristorcelli, Buoyancy-driven variable-density turbulence, *J. Fluid Mech.* **591**, 43 (2007).
- [39] C. E. Leith, Diffusion approximation to inertial energy transfer in isotropic turbulence, *Phys. Fluids* **10**, 1409 (1967).
- [40] D. A. Drew and S. L. Passman, *Theory of Multicomponent Fluids* (Springer, New York, NY, 2006), Vol. 135.
- [41] B.-J. Gréa, The rapid acceleration model and the growth rate of a turbulent mixing zone induced by Rayleigh–Taylor instability, *Phys. Fluids* **25**, 015118 (2013).
- [42] S. S. Girimaji, On the modeling of scalar diffusion in isotropic turbulence, *Phys. Fluids A* **4**, 2529 (1992).
- [43] D. Anderson, J. Tannehill, and R. Pletcher, *Computational Fluid Mechanics and Heat Transfer* (CRC Press, Boca Raton, 1984).
- [44] J. Crank and P. Nicolson, A practical method for numerical evaluation of solutions of partial differential equations of the heat-conduction type, in *Mathematical Proceedings of the Cambridge Philosophical Society* (Cambridge University Press, Cambridge, 1947), Vol. 43, pp. 50–67.
- [45] D. Aslangil, D. Livescu, and A. Banerjee, Atwood and Reynolds numbers effects on the evolution of buoyancy-driven homogeneous variable-density turbulence (unpublished).
- [46] T. D. Lee, On some statistical properties of hydrodynamical and magneto-hydrodynamical fields, *Q. Appl. Math.* **10**, 69 (1952).
- [47] D. Livescu, J. Mohd-Yusof, M. R. Petersen, and J. W. Grove, Cfdns: A computer code for direct numerical simulation of turbulent flows, Los Alamos National Laboratory Technical Report No. LA-CC-09-100 (2009).
- [48] D. Livescu, Numerical simulations of two-fluid turbulent mixing at large density ratios and applications to the Rayleigh–Taylor instability, *Phil. Trans. R. Soc. A* **371**, 20120185 (2013).

- [49] T. T. Clark, S.-Y. Chen, L. Turner, and C. Zemach, Turbulence and turbulence spectra in complex fluid flows, Technical Report, Los Alamos National Laboratory (1997).
- [50] K. Pearson, *Karl Pearson's Early Statistical Papers*, edited by E. S. Pearson (Cambridge University Press, 1956).